Title

Optimization of an on-board imaging system for extremely rapid radiation therapy.

Permalink

https://escholarship.org/uc/item/3dr962dw

Journal

Medical Physics, 42(11)

Authors

Cherry Kemmerling, Erica

Wu, Meng

Yang, He

et al.

Publication Date

2015-11-01

DOI

10.1118/1.4934377

Peer reviewed

Optimization of an on-board imaging system for extremely rapid radiation therapy

Erica M. Cherry Kemmerling, Meng Wu,[a)] and He Yang
Department of Radiology, Stanford University, Stanford, California 94305

Peter G. Maxim and Billy W. Loo, Jr.
Department of Radiation Oncology, Stanford University, Stanford, California 94305 and Stanford Cancer Institute, Stanford University School of Medicine, Stanford, California 94305

Rebecca Fahrig
Department of Radiology, Stanford University, Stanford, California 94305

Purpose: Next-generation extremely rapid radiation therapy systems could mitigate the need for motion management, improve patient comfort during the treatment, and increase patient throughput for cost effectiveness. Such systems require an on-board imaging system that is competitively priced, fast, and of sufficiently high quality to allow good registration between the image taken on the day of treatment and the image taken the day of treatment planning. In this study, three different detectors for a custom on-board CT system were investigated to select the best design for integration with an extremely rapid radiation therapy system.
Methods: Three different CT detectors are proposed: low-resolution (all 4×4 mm pixels), medium-resolution (a combination of 4×4 mm pixels and 2×2 mm pixels), and high-resolution (all 1×1 mm pixels). An in-house program was used to generate projection images of a numerical anthropomorphic phantom and to reconstruct the projections into CT datasets, henceforth called "realistic" images. Scatter was calculated using a separate Monte Carlo simulation, and the model included an antiscatter grid and bowtie filter. Diagnostic-quality images of the phantom were generated to represent the patient scan at the time of treatment planning. Commercial deformable registration software was used to register the diagnostic-quality scan to images produced by the various on-board detector configurations. The deformation fields were compared against a "gold standard" deformation field generated by registering initial and deformed images of the numerical phantoms that were used to make the diagnostic and treatment-day images. Registrations of on-board imaging system data were judged by the amount their deformation fields differed from the corresponding gold standard deformation fields—the smaller the difference, the better the system. To evaluate the registrations, the pointwise distance between gold standard and realistic registration deformation fields was computed.
Results: By most global metrics (e.g., mean, median, and maximum pointwise distance), the high-resolution detector had the best performance but the medium-resolution detector was comparable. For all medium- and high-resolution detector registrations, mean error between the realistic and gold standard deformation fields was less than 4 mm. By pointwise metrics (e.g., tracking a small lesion), the high- and medium-resolution detectors performed similarly. For these detectors, the smallest error between the realistic and gold standard registrations was 0.6 mm and the largest error was 3.6 mm.
Conclusions: The medium-resolution CT detector was selected as the best for an extremely rapid radiation therapy system. In essentially all test cases, data from this detector produced a significantly better registration than data from the low-resolution detector and a comparable registration to data from the high-resolution detector. The medium-resolution detector provides an appropriate compromise between registration accuracy and system cost. © *2015 American Association of Physicists in Medicine.* [http://dx.doi.org/10.1118/1.4934377]

Key words: CT, radiotherapy, on-board imaging, Monte Carlo, registration

1. INTRODUCTION

1.A. Background

One of the biggest challenges in radiotherapy is motion management. If a patient is positioned differently on the day of treatment delivery than on the day of treatment planning (interfraction motion) or moves during a treatment (intrafraction motion), radiation can miss the target and damage healthy tissue. Strategies for motion management are numerous and varied, but they fall into two major categories: techniques that minimize patient motion (catheter insertion, breath holding, and immobilization devices) and techniques that either track patient motion or turn the radiation on only when the patient is in a specific position (beam gating, active breath control, beam tracking, and use of implanted markers). All of these techniques are discussed extensively elsewhere.[1–5]
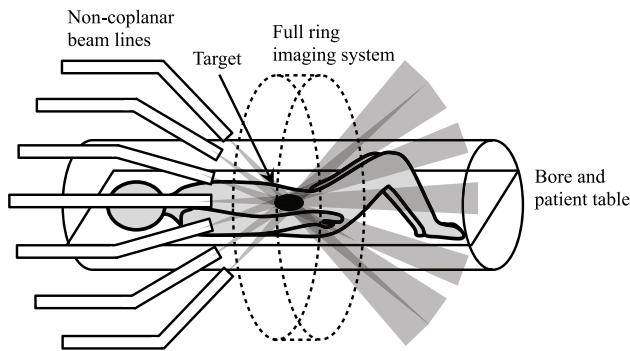
FIG. 1. Extremely rapid radiation therapy setup. Stationary beam lines irradiate a target from multiple angles. The on-board imaging system location is indicated by the dotted lines. The noncoplanar geometry of the treatment beam lines ensures the imaging and treatment hardware do not interfere.

An interesting solution to the radiotherapy motion management problem is to deliver the treatment so rapidly that the patient has no time to move. The details of one such system are explained elsewhere,[6–8] but in brief, the radiation is supplied by a multipronged, stationary, noncoplanar beam line system shown in Fig. 1. The multiple beam lines make gantry motion unnecessary, and a full dose of radiation can be delivered in less than the time frame of physiologic motion, for example, within a single breath hold. This process could be up to two orders of magnitude faster than current state-of-the-art radiotherapy systems. Additionally, the noncoplanar beam geometry allows incorporation of a full-ring, large bore imaging system that does not interfere with the treatment equipment, as shown in Fig. 1.

Extremely rapid radiation therapy systems will eliminate the need for intrafraction motion management, but interfraction motion management is still required. Thus, an imaging system to align the patient must be developed and incorporated into such setups. Current state-of-the-art radiotherapy systems almost always use cone beam CT (CBCT) systems to image and align the patient prior to treatment.[9] On-board CBCT systems have been shown to produce good enough image quality to identify critical features of the patient's position in the vast majority of cases.[10–12] However, gantry rotation speed is limited, and this can introduce significant motion artifacts.[11]

Once a cone-beam image of the patient has been acquired, the image must be registered to the treatment plan, which is generally based on a diagnostic-quality CT scan taken days or weeks earlier. The patient is then manually manipulated (and sometimes immobilized) to match their position on the day their diagnostic treatment-planning image was taken. Many methods have been developed to perform this registration and treatment plan adaptation.[14–18] The imaging system discussed in this work will allow adaptation of the treatment to the patient's daily position instead of the other way around, increasing treatment speed and patient comfort. Most importantly, however, this modification will increase treatment accuracy, as it has been shown that adapting radiotherapy treatments to the current patient position produces more accurate treatment plans than manipulating patients to match previous positions.[19]

The success of the registration between the diagnostic and on-board imaging system scans is an important metric of the

success of the imaging system; if the registration is perfect, the treatment plan can, in theory (the process of accurately adapting treatment contours to a deformed 3D volume is a separate problem that will not be addressed in this work but has been studied extensively by others[16,18,20]), be perfectly adapted to the patient's current position. Thus, a natural way to evaluate the effectiveness of an on-board imaging system is to investigate a widely used registration algorithm's success in registering images taken by the system in question with images taken by a clinical CT system.

The primary goal in designing an on-board imaging system for an extremely rapid radiation therapy system is to retain the advantages of a state-of-the-art on-board CBCT imaging system without negating the advantages of the fast treatment and large treatment field of view offered by the multiple stationary beam lines. Commercial on-board CBCT systems are unsuitable for this application because image acquisition takes too long. The current work investigates the design and optimization of an alternate on-board CT system suitable for an extremely rapid radiation therapy. Section 1.B will discuss the workflow and specific requirements of the imaging system, describe a simulation designed to evaluate the success of three potential imaging system designs, and use a commercial registration tool to evaluate the success of the three systems and recommend one for further investigation.

1.B. System design and workflow

A proposed workflow for extremely rapid radiation therapy is summarized in Fig. 2. First, a radiation oncologist plans the treatment using a diagnostic-quality CT scan, which will henceforth be called "phase 1 imaging." For the purposes of this study, it is assumed that the phase 1 diagnostic-quality scan is taken with a state-of-the-art, multislice CT scanner. On the day of the treatment, a helical CT of the patient (artifact-free and with a large field of view, but requiring several seconds) is acquired with the on-board imaging system (phase 2 imaging) and the prior phase 1 diagnostic-quality scan is registered to this image, allowing adaptation of the treatment plan. Phase 2 imaging will be conducted like a standard helical CT scan— the patient table will translate as the source rotates. The motion artifacts produced by this imaging phase are expected to be no larger than motion artifacts in a typical diagnostic CT scan. Finally, an axial CT image (fast but lower quality) is acquired (phase 3 imaging) and the phase 2 helical image is registered to this image to make sure the patient has not moved significantly in the time it took to adapt the treatment plan. After it is confirmed that the patient has not moved, the treatment is delivered.

The motivation for the two-part on-board imaging workflow is that it is currently impractical to assume that a large 3D volume can be deformably registered and a radiotherapy treatment replanned in the same breathhold during which the treatment is delivered. It is much more tractable to design a system in which the patient can breathe freely while replanning takes place. The phase 2 helical imaging and treatment adaptation are meant to account for large deformations that could occur over a period of days or weeks, such as weight loss, large

Prior to treatment:

Phase 1 imaging: Radiotherapy simulation

Day of treatment:

Phase 2 imaging: *Phase 3 imaging:*
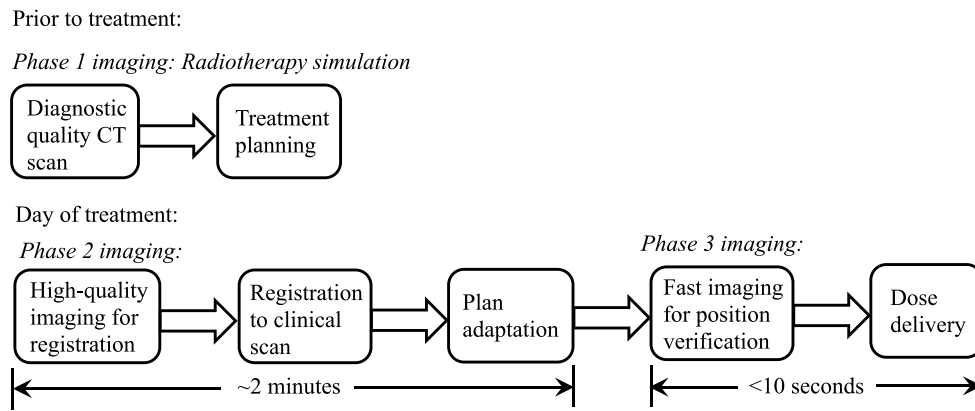
FIG. 2. Extremely rapid radiation therapy workflow. Two minutes may be an optimistic estimate for phase 2 imaging, but it is expected to be increasingly straightforward in the next few years as computing power and algorithms improve.

differences in volumes of deformable organs like the stomach, bladder, bowel, and tumor growth or shrinkage. Because the differences between the phase 1 and phase 2 images could be significant, it is expected that registration and replanning would take a minimum of 1 min, and the patient would need to breathe during this time. Very little is expected to change between imaging phases 2 and 3, particularly if the patient is told to hold his or her breath during both scans, and thus, the registration and check that no significant motion has occurred should take no more than a few seconds. This will allow the treatment to be delivered in the same breathhold as the phase 3 axial image acquisition. Optimal registration and replanning are themselves challenges to be addressed in future work, particularly the registration of phase 2 and phase 3 images, which have different fields of view.

We propose to use the same hardware for both phases of the on-board imaging, despite the fact that the goals of the two phases differ significantly. The goal of phase 2 helical imaging is to acquire a high-quality image without artifacts that encompasses the entire treatment volume. This will circumvent the major problem of cone beam artifacts created by traditional on-board imaging systems. Ideally, the phase 2 image would be acquired within a breathhold to minimize motion artifacts, but speed is not the most important parameter. The goal of

phase 3 axial imaging is to image as fast as possible in order to fit the image acquisition, registration, and treatment into a single breathhold. The acquired phase 3 image can have a smaller field of view and does not need to be high quality as long as important features can be identified. It is also important to minimize component costs of the imaging system so that overall system cost is contained.

To meet all of these objectives, we have designed a custom CT system with a large detector and a source that can be collimated to various numbers of rows. The system will operate at a standard CT rotation speed of 60 rpm, and the detector will have a frame rate of at least 1000 frames/s. The detailed parameters of the system are listed in Table I. Some parameters, such as field of view and bore size, were selected to optimize the flexibility of the device in treating large patients and patients with extended and/or complex-shaped tumors. Other parameters, such as the bowtie filter and antiscatter grid, were designed to be similar to state-of-the-art CT equipment. The phase 2 helical and phase 3 axial images will be acquired using the same CT detector, but for phase 2 helical imaging, only the middle third of the detector will be illuminated. This will ensure that the phase 2 image is free of cone beam artifacts. The three-phase imaging workflow will not necessarily deliver a higher patient dose than systems that take only one CBCT

TABLE I. Comparison of typical imaging systems with the proposed custom system.

Property	Typical clinical CT	Typical on-board CBCT	Custom on-board system
Source to detector distance (mm)	1040	1400–1700 (Ref. 21)	1300
Source to axis distance	570 mm	1000 mm (Ref. 21)	650
Detector size	64×1000 pixels	768×1024 pixels	a
Detector pixel size	1×1 mm	0.4×0.4 mm	a
Antiscatter grid	2D, 35 mm-tall, 80 μm-thick lamellae	b	2D, 35 mm-tall, 80 μm-thick lamellae
Source spectrum	120 kVp tungsten target	120 kVp tungsten target	120 kVp, tungsten target
Bore size	600 mm	N/A c	900 mm
In-plane field of view (mm)	500	240 (Ref. 11) to 450 (Ref. 21)	500
Axial field of view (at isocenter) (mm)	32	175 (Ref. 10)	100
Bowtie filter	b	b	1–10 mm Al, thickness varies with angle
Helical pitch	0.5–0.9	N/A	0.75

[a]Investigated in this study.
[b]Information is proprietary.
[c]Most on-board CBCT systems are open-bore.

scan prior to each treatment, because the different detector designs allow acquisition of similar image quality to on-board CBCT with a lower total photon flux. Dose/image-quality optimization for this imaging protocol will be addressed in a separate publication.

In this study, we focus on optimizing the design of the detector, which will likely be the most expensive component of the imaging system and will play an important role in determining the image quality. The overall goal is to design a detector with low component costs that still provides sufficient image quality such that day-of-treatment images can be reliably registered to previous scans. In particular, the phase 1 diagnostic-quality images must be correctly registered to the phase 2 helical images and the phase 2 helical images must be correctly registered to the phase 3 axial images.

We examine three detector designs. All three are curved and have the same dimensions: a radius of 1300 mm, an arclength of 1024 mm, and a height of 192 mm. Each detector is designed to work for both phase 2 and phase 3 imaging. During phase 2 helical imaging, the source is collimated to a cone angle of 2.9° and illuminates only the middle third of the detector. During phase 3 axial imaging, the source has a cone angle of 9.6° and illuminates the entire detector. The low-resolution detector consists of 48 rows of 4×4 mm pixels with 256 pixels per row for a total of 12 288 pixels. With fewest pixels, it provides lower resolution but is also low cost. The medium-resolution detector has 64 rows of pixels, 16 rows of 4×4 mm pixels with 256 pixels per row followed by 32 rows of 2×2 mm pixels with 512 pixels per row followed by another 16 rows of 4×4 mm pixels with 256 pixels per row. It has a total of 24 576 pixels and is the intermediate-cost detector. These pixel sizes were chosen to be comparable to clinically used resolutions for CBCT image guidance systems in radiation therapy. The high-resolution detector has 192 rows of uniformly spaced 1×1 mm pixels with 1024 pixels in each row for a total of 196 608 pixels. This is the most expensive detector design and is expected to produce the highest resolution images for both imaging phases. Its resolution is comparable to that of a clinical CT scanner.

2. METHODS

2.A. Numerical simulations and registration

A series of numerical simulations were performed to evaluate the image quality that could be obtained from the three different detectors. The purpose of these simulations was to generate realistic data from each system that would allow evaluation of the registration success at the different phases of the workflow. A male humanoid XCAT numerical phantom made of cubic voxels was used for all simulations.[22] We chose to focus on abdominal imaging, where the soft-tissue image contrast is low and thus deformable registration is most challenging. Most of the organ sizes were left at their default values, but the volumes of the stomach, bladder, and lungs were changed between the imaging phase 1 (diagnostic-quality) and phase 2 (helical) simulations to simulate realistic day-to-day patient deformation. Only the volume of the lungs was changed between imaging phases 2 (helical) and 3 (axial), since the patient's stomach and bladder would not change volume significantly within a few minutes. These changes in phantom organ size are representative rather than all encompassing—in a real patient, comparable deformations could also occur due to other factors such as the motion of gas in the bowel. Table II summarizes the phantom parameters for each simulation.

In order to establish whether the imaging systems permit registration of small lesions, three spherical, 5-mm-diameter lesions were added manually to the liver in each phantom. The lesions were 5% denser, 10% denser, and 5% less dense than the surrounding liver tissue. The positions of the lesions relative to each other and to the edges of the liver were kept consistent between the variously deformed phantoms.

2.B. Primary projection image generation

The primary photon projection images were generated using an in-house MATLAB-based code that receives a polychromatic spectrum and a voxelized phantom as input and calculates the attenuation line integral of rays passing through the phantom using the separable footprints method.[23] For each 360° rotation of the source and detector, 720 projection images were generated, and the starting angle was the same every time. For these simulations, the XCAT phantoms described in Table II were generated at a resolution of 0.6 mm cubic voxels and segmented into five materials: lung, soft tissue, muscle, blood, and cortical bone. Material properties were obtained from the NIST database. ("Tables of X-ray Mass Attenuation Coefficients and Mass Energy-Absorption Coefficients," http://www.nist.gov/pml/data/xraycoef/, accessed: October 1, 2013.) An aluminum bowtie filter was included to reduce skin dose. The shape of the bowtie filter is described by Eq. (1), which relates the thickness, T, to the fan angle, θ. The units are millimeter,

TABLE II. Phantom parameters. Large patient deformations occur between the phase 1 diagnostic-quality scan and the phase 2 helical scan. Only a small deformation occurs between the phase 2 helical scan and the phase 3 axial scan. All respiratory phases are for natural breathing.

Imaging phase	Respiratory phase	Stomach volume (ml)	Bladder volume (ml)
1 (diagnostic-quality)	0.0 (full exhale)	500	150
2 (helical)	0.4 (full inhale)	1000	300
3 (axial)	0.2	1000	300

$$T(\theta) = 1 + 4.5(1 - \cos(8\theta)). \tag{1}$$

Automatic exposure control was implemented based on the model suggested by Gies *et al.*[24] The exposure used was approximately 330 mAs for the phase 2 helical scans and 33 mAs for the phase 3 axial scans. The total exposure used, approximately 363 mAs, was within the typical range used by on-board CBCT systems.[10–12] Based on previous dose measurements for similar setups, it is estimated that the phase 2 helical scan would expose the illuminated tissue to 6.0–8.9 mGy and the phase 3 axial scan would expose illuminated tissue to 0.6–0.9 mGy.[13]

The detectors were energy integrating, and the geometric efficiency of the detectors varied from 0.8 to 0.95 depending on the size of the pixels and the presence of the antiscatter grid. The grid consisted of 80-μm-thick lamellae surrounding each pixel and was assumed to be perfectly absorbing. Quantum noise and a modeled point spread function were added to the images by adding simple Poisson noise and blurring with a 2D Gaussian kernel of 0.6 mm standard deviation. The Gaussian blurring accounts for both the finite focal spot size and detector cross talk.

2.C. Scatter projection image generation

The scatter in the projection images was modeled using a Monte Carlo simulation based on MC-GPU, an open-source Monte Carlo framework that uses the PENELOPE 2006 physics engine to model particle interactions. Details and validation of this software are described elsewhere.[25] MC-GPU generates projection images of a numerical phantom onto a flat-panel detector. The user specifies the source spectrum, voxelized phantom, system geometry, and detector parameters. For this study, three new features were added to the program. First, the flat-panel detector was transformed to a curved detector. This was accomplished by detecting the location and direction at which each photon hit the flat-panel detector built into the simulation and mapping its path backward until it intersected the curved detector. The photon was then binned in the correct pixel based on its location on the curved detector. The second feature added to the default MC-GPU code was a perfectly absorbing antiscatter grid. The grid was 2D and consisted of 35-mm-tall lamellae surrounding each detector pixel. The lamellae were tilted toward the source to minimize absorption of primary photons. The grid was implemented by tracing the path of each photon hitting the detector backward until it either intersected a grid lamella or passed all grid lamellae. In the former case, the photon was not scored on the detector.

The final feature added to MC-GPU was the bowtie filter specified by Eq. (1). The MC-GPU framework does not allow parts of the phantom (such as a bowtie filter) to move with the source between projections, so an alternative bowtie filter representation method was developed. This method is summarized below.

(1) Ten 120 kVp tungsten target x-ray spectra were generated using SPEKTR.[26] The spectra were filtered with 1, 2, 3 mm, etc., of aluminum.

(2) The spectra were subtracted to obtain the difference spectrum between 1 and 2 mm Al filtration, 2 and 3 mm Al filtration, etc. Henceforth, these spectra will be called the "difference spectra."

(3) One complete scatter simulation was performed using the spectrum filtered with 10 mm aluminum. The x-ray source was collimated to cover the entire detector.

(4) A second complete scatter simulation was performed using the 9/10 mm difference spectrum as the x-ray source. The source was collimated to cover all fan angles filtered by less than 9.5 mm Al. The number of particles used was scaled to reflect the smaller source divergence and the smaller total flux of the 9/10 mm difference spectrum compared with the 10 mm spectrum.

(5) A third complete scatter simulation was performed using the 8/9 mm difference spectrum. The source was collimated to cover all fan angles filtered by less than 8.5 mm Al and the same photon number scaling described in step 4 was performed.

(6) The process was continued with steps similar to steps 4 and 5 until all difference spectra were used. The ten datasets were summed to make a complete scatter dataset with a bowtie filter.

In a separate validation study, the scatter in two projection images using this method was compared with the scatter in projections of phantoms that included a voxelized aluminum bowtie phantom with the shape given by Eq. (1). The medium-resolution detector from the current study was used. In both cases, the total scatter differed by less than 2% and the scatter averaged over regions of 4×4 pixels differed by less than 5%.

MC-GPU generates primary images as well as scatter images, so in the current study, the scatter images were scaled by multiplying them by the ratio of the average attenuated pixel intensity in the in-house primary projections to that of the MC-GPU primary projections. Finally, the scaled scatter datasets were added to the primary projection images to make raw datasets.

2.D. Postprocessing and reconstruction

Prior to reconstruction, the projection images were corrected for scatter. An estimate of the scatter across the entire image was obtained by linearly interpolating the scatter on the top and bottom rows of the detector. In a physical system, this scatter could be measured by collimating the source such that no primary rays reach the top and bottom detector rows.[27] The scatter estimate was subtracted from the raw projection images. The images were then normalized and their logarithm was computed.

Next, the beam hardening in the projection images was corrected using a polynomial-based water beam-hardening correction. The correction was done on a pixel-by-pixel basis to account for the effect of the bowtie filter. The axial scan data were reconstructed using a standard FDK method[28] with a Hamming windowed Ram-Lak kernel. The helical data were reconstructed using a standard FDK-type filtered back

projection for helical CT.[29] Parker weighting and 3D weighting were used to reduce helical and cone beam artifacts in the reconstructions.[30] The weighting functions were not optimized for the geometry, but they nevertheless improved the image quality. A water cylinder-fitting algorithm was implemented to extend the field of view and reduce truncation artifacts.[31,32]

2.E. Registration

The reconstructed images were loaded into MIM MAESTRO registration software (MIM Software, Inc., http://www.mimso ftware.com/, version 6.5). MIM is just one of many validated registration options,[33] and it was chosen for its common use in clinical settings. For each detector setup, the reconstructed phase 1 diagnostic-quality image (source) was registered to the phase 2 helical image (target) and the phase 2 helical image (source) was registered to the phase 3 axial image (target). All registrations were performed using MIM's built-in deformable registration with the field of view cropped to a 270 ×240 mm region surrounding the abdomen. The registered images and 3D deformation field were loaded into MATLAB using MIM's MATLAB image-deform extension. The 3D deformation field was interpolated to obtain a vector field representing the displacement between the center of each voxel in the source image and its corresponding location in the target image.

To establish a ground truth for registration, the three numerical phantoms summarized in Table II were converted to HU, cropped to the correct fields of view for the three imaging phases, and deformably registered using the same method as described above. These registrations will henceforth be called "gold standard" registrations, as opposed to "realistic" registrations, which use simulation data. The two gold standard registrations represent the best possible cases for registering imaging phase 1 to phase 2 and phase 2 to phase 3. They are equivalent to registrations of perfect CT datasets with no blurring mechanisms, noise, scatter, or artifacts. The realistic registrations were compared with the gold standard registrations to evaluate their quality, a process described in more detail in Sec. 3.

3. RESULTS

3.A. Qualitative reconstruction and registration results

Figure 3 shows sample reconstructed axial slices for the three detectors. The top row shows a typical slice from the
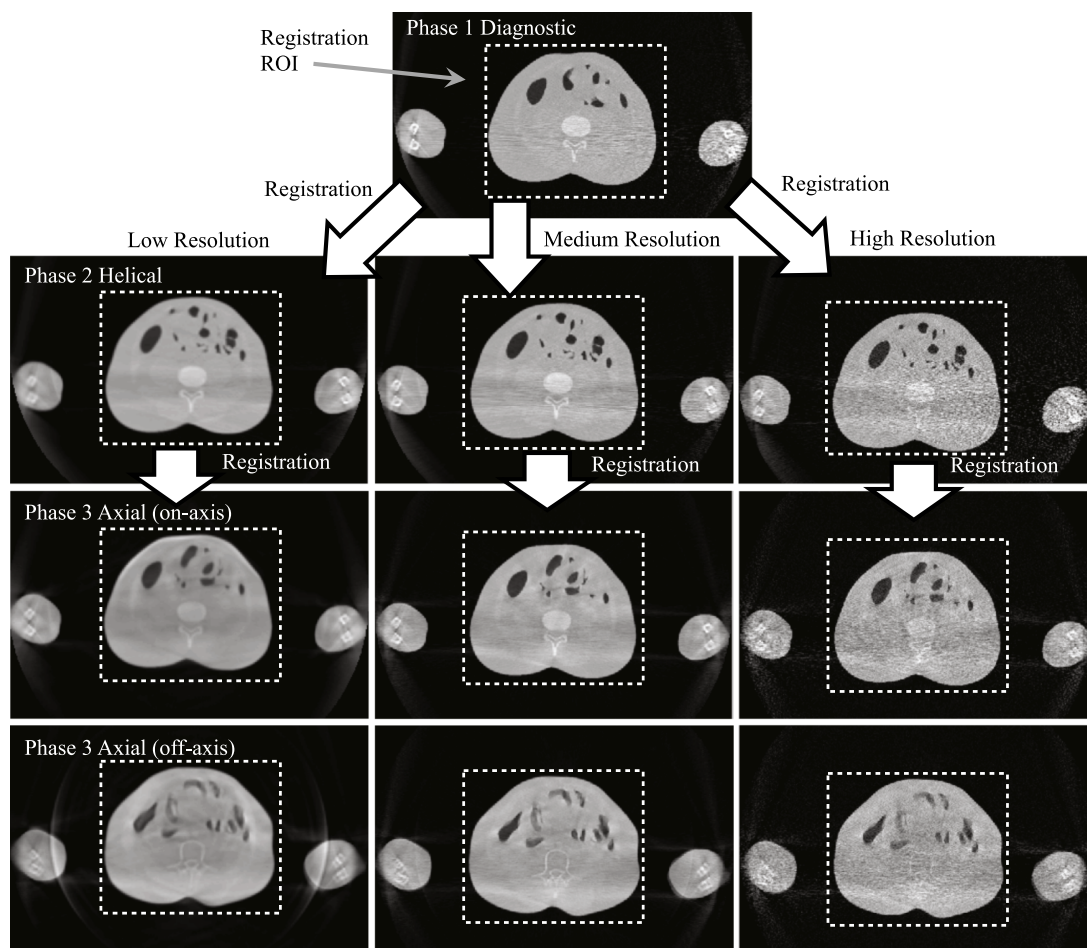

FIG. 3. Representative axial slices of reconstructed data. Each column contains images from a different detector design. The top image is typical diagnostic-quality scan data (imaging phase 1). The middle row is typical helical scan data (imaging phase 2). The bottom two rows are central and off-axis slices of axial scan data (imaging phase 3). White boxes indicate the ROI used for registration.
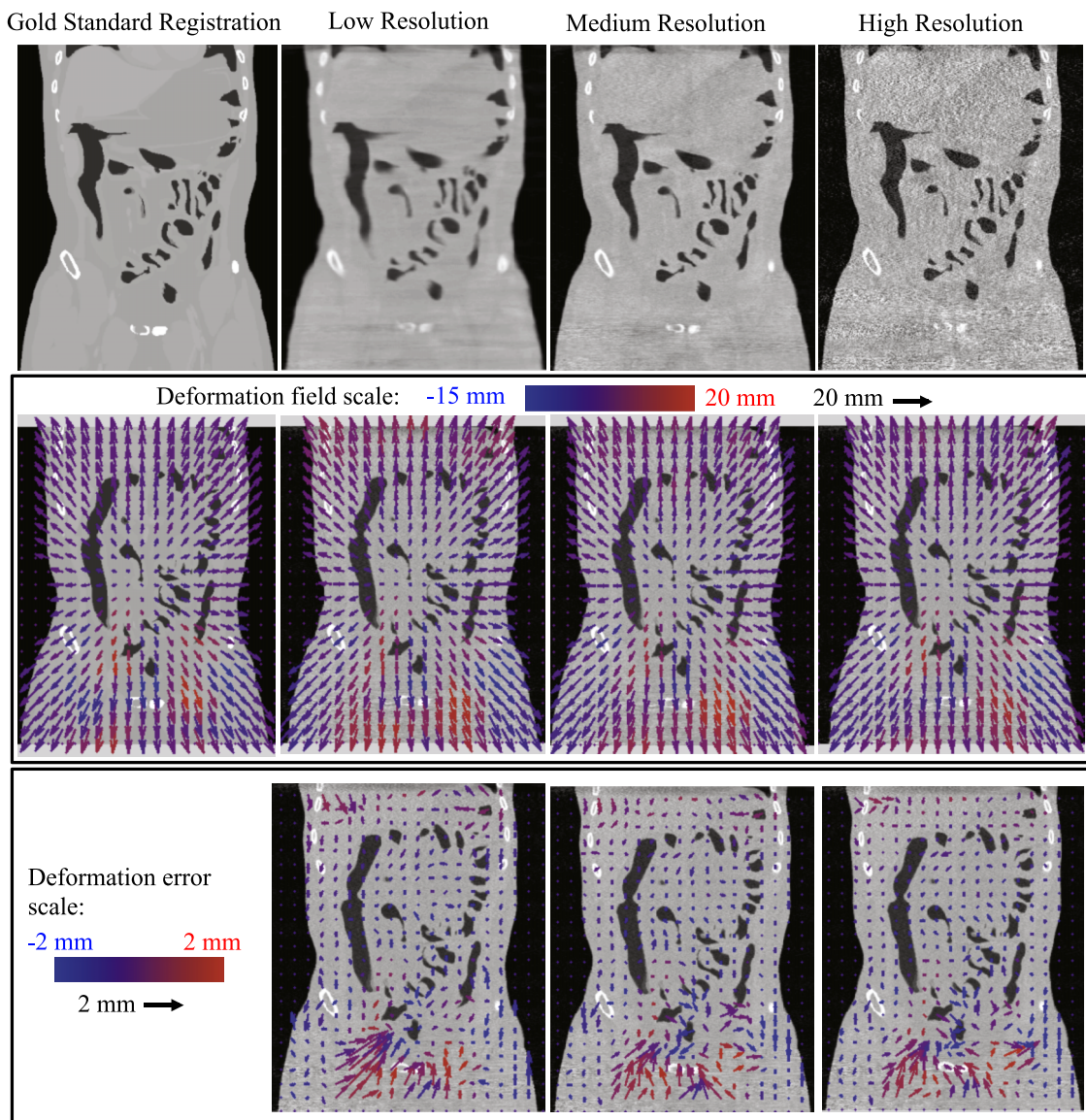
FIG. 4. Representative coronal slices of the phase 1 (diagnostic-quality)/phase 2 (helical) registration. The top row shows target images from the different detectors. The middle row shows corresponding source images and deformation fields. The bottom row shows the difference between each realistic deformation field and the gold standard deformation field. Each vector points from a point in the source image to its corresponding location in the target image. Vector lengths indicate in-plane deformation and colors indicate out-of-plane deformation. Red is out of the page. Color and reference vector length scales are shown for each image row. Note the scales for the middle and bottom image rows are not the same. The low-resolution deformation field contains the most error and the medium- and high-resolution deformation fields are comparable.

phase 1 diagnostic-quality scan and the second row shows typical slices from the phase 2 helical scan. The bottom two rows show central slices from the phase 3 axial scan and slices from the very edge of the axial field of view. As expected, the images from the low-resolution detector demonstrate blurring and smoothing while the data from the high-resolution detector are sharpest but noisiest. The high-resolution detector data are far noisier than would be expected for a clinical CT scanner with detector pixels of the same size because the three detectors in the current study are compared at the same total exposure (in milliampere per second) and that exposure is similar to that of a typical on-board CBCT scan. The purpose of the on-board imaging system is not to produce images for diagnostics but to produce images that register well; therefore, limiting patient dose is more important than lowering noise.

Noise and artifacts dominate the texture of all reconstructed slices because the XCAT phantom contains no intraorgan density variation. This could degrade the quality of the registration because MIM is known to perform better on textured surfaces.[34]

All helical and axial scan images in Fig. 3 exhibit some artifacts. One of the most significant artifacts is the signal decrease between the upper limbs caused by beam hardening in the limb bones. This artifact is corrected poorly by the beam-hardening correction algorithm because bone and water have dissimilar properties. In addition, all reconstructions have truncation artifacts near the edges of the field of view. These artifacts are minor due to the imaging system's large field of view and the applied truncation correction. The last significant artifact is a cone beam artifact, which can be seen in the last row

TABLE III. Pointwise distances between the realistic deformation fields and the corresponding gold standard deformation fields. The low-resolution detector setup has more error than the medium- and high-resolution setups. The medium- and high-resolution setups produce comparable-quality registrations.

Setup	Phase 1 (diagnostic)/phase 2 (helical) registration pointwise distance (mm)		Phase 2 (helical)/phase 3 (axial) registration pointwise distance (mm)	
Low-resolution detector	Minimum:	0.0	Minimum:	0.0
	Median:	2.4	Median:	4.0
	Mean:	3.1	Mean:	4.8
	Maximum:	27.8	Maximum:	21.2
Medium-resolution detector	Minimum:	0.0	Minimum:	0.0
	Median:	2.0	Median:	3.3
	Mean:	2.6	Mean:	3.9
	Maximum:	21.7	Maximum:	17.4
High-resolution detector	Minimum:	0.0	Minimum:	0.0
	Median:	1.7	Median:	3.1
	Mean:	2.0	Mean:	3.9
	Maximum:	21.1	Maximum:	18.0

of images. The edge slice of the axial scan low-resolution detector reconstruction (lower left) has a particularly prominent artifact caused by truncation in the z-direction and exacerbated by the large detector pixel size.

Because high-speed radiotherapy systems will primarily target body tumors and because truncation artifacts could significantly affect the quality of the registration, only the body of the phantom was included in the registrations. The ROI used for registration is outlined in each of the images in Fig. 3.

Figure 4 shows representative coronal slices of the phase 1 (diagnostic-quality)/phase 2 (helical) registration (quantitative values for these data are listed in Table III and will be discussed later in the text). The top row of Fig. 4 shows one slice of the registration target image for each detector case (phase 2 reconstructed helical scan data), and the middle and bottom rows show corresponding slices from the source images. For the gold standard case, the bottom slices are part of the phase 1 phantom, and for the other cases, they are part of the diagnostic-quality phase 1 reconstruction. In the middle row of images, phase 1 slices are superimposed with a vector field that

maps points in the source image to their corresponding points in the target image. All vector fields have had their mean values subtracted to remove the effect of translation between images. The bottom row shows the difference between each detector's deformation field and the gold standard deformation field.

The overwhelming feature of all four deformation vector fields is an expansion centered at the center of the phantom. This is expected because the phase 2 phantom has larger stomach, lung, and bladder volumes than the phase 1 phantom, so the phase 1 phantom must expand to match the phase 2 phantom.

A useful evaluation metric for registration data is a comparison between realistic and gold standard deformation fields. This comparison isolates the quality of the imaging system from factors such as the registration algorithm's performance and the details of the phantoms. The less a realistic registration's deformation field differs from the gold standard registration, the better it is. Qualitatively, all three realistic datasets in Fig. 4 produce good registration results. The deformation field for the low-resolution detector seems to have the
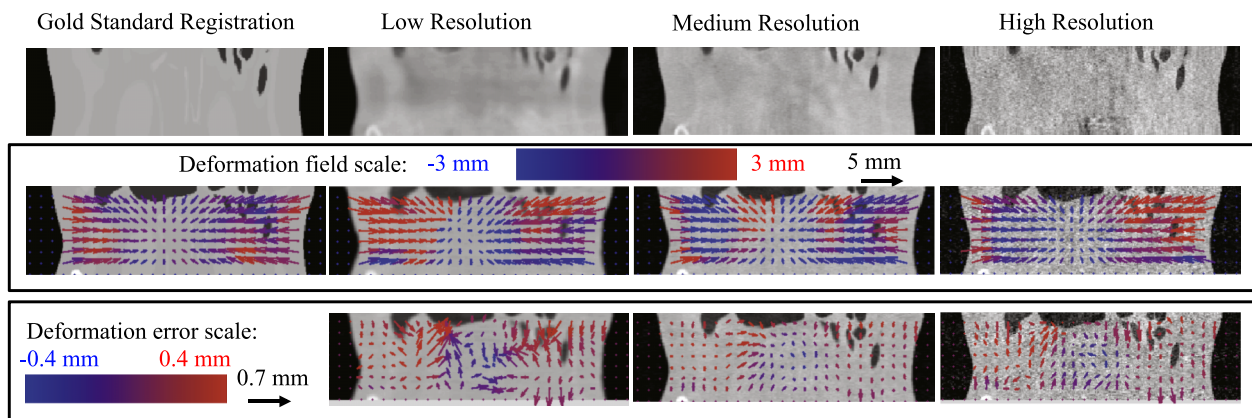

FIG. 5. Representative coronal slices of the phase 2 (helical)/phase 3 (axial) registration. The top row shows target images from the different detectors. The middle row shows corresponding source images and deformation fields. The bottom row shows the difference between each realistic deformation field and the gold standard deformation field. Each vector points from a point in the source image to its corresponding location in the target image. Vector lengths indicate in-plane deformation and colors indicate out-of-plane deformation. Red is out of the page. Color and reference vector length scales are shown for each image row. Note the scales for the middle and bottom image rows are not the same. The medium-resolution deformation field shows the least error but the high-resolution deformation field is comparable.

most error, with large in-plane errors in the lower abdomen and overestimation of the out-of-plane deformation near the top of the slice. The deformation fields for the medium and high-resolution detectors match the gold standard vector field comparably well. These features were similar in other slices of the 3D deformation field.

Figure 5 shows representative coronal slices of the phase 2 (helical)/phase 3 (axial) registrations. The layout is the same as in Fig. 4, but the deformation vectors are far smaller in magnitude than in Fig. 4. This is expected because the only difference between the phase 2 and phase 3 phantoms is their lung volumes, and even this difference is not as great as the difference in lung volumes between the phase 1 and phase 2 phantoms. The most prominent feature of all four vector fields is an in-plane contraction, likely caused by this reduction in lung volume. Although the in-plane vector field shapes agree well between all four datasets, the agreement is poor in the out-of-plane direction, and none of the three realistic deformation

fields resembles the gold standard deformation field better than the others. However, it must be noted that the out of plane deformation vectors are far smaller than those plotted in Fig. 4, so the absolute errors are not much worse than in the phase 1/phase 2 registration. The deformation error images show that the medium-resolution detector performs best, but the high-resolution detector produces a comparable-quality registration. The low-resolution detector data's registration error is, on average, much higher.

3.B. Global registration evaluation

The overall quality of each deformable registration was quantitatively evaluated by calculating the pointwise distance between each vector in the deformation field and its corresponding vector in the gold standard deformation field. Pointwise distance D between two vector fields a and b at point (x,y,z) is defined by Eq. (2),

$$D(x,y,z) = \sqrt{(a_x(x,y,z) - b_x(x,y,z))^2 + (a_y(x,y,z) - b_y(x,y,z))^2 + (a_z(x,y,z) - b_z(x,y,z))^2}. \tag{2}$$

Table III summarizes the minimum, maximum, mean, and median pointwise distance for all datasets. Points outside of the body are not included in these statistics.

Although each dataset has a few outlier points, as shown by the high maximum errors, all three phase 1 (diagnostic-quality)/phase 2 (helical) registrations had mean and median errors less than 3.2 mm. The high-resolution detector performed best, but the medium-resolution detector performed worse by only a fraction of a millimeter in both the mean and median errors. The phase 2 (helical)/phase 3 (axial) registration errors are uniformly higher than the phase 1/phase 2 errors, likely due to the lower image quality of the axial scans. It is particularly notable that the low-resolution detector had a mean error of 4.8 mm, nearly the diameter of the phantoms' spherical liver lesions. This result is unacceptable, as it would mean the registration would have a good chance of mapping an entire 5-mm lesion to the wrong location in the body. The

medium- and high-resolution detectors performed somewhat better in the phase 2/phase 3 registration and the magnitudes of their errors were comparable.

3.C. Point of interest registration evaluation

One of the goals of the imaging and registration workflow is to track the motion of small lesions, so it is instructive to examine the spherical liver lesion images in detail. Table IV summarizes the contrast to noise ratio (CNR) and apparent width of the three lesions in each imaging scenario. As expected, the CNR decreases monotonically as pixel size increases, and CNR is significantly better in the phase 2 images than the phase 3 images. This is reasonable because the exposure is much higher during phase 2 than phase 3. The effective width of the lesion images is higher for the low-resolution detector, which is expected since the image is blurred over larger pixels.

TABLE IV. Imaging statistics for the three low-contrast liver lesions. Contrast to noise ratios were calculated by subtracting the average CT number in each lesion from the average CT number in surrounding liver tissue and dividing by the standard deviation of the CT number in nonlesion liver tissue. Sigmas were calculated by fitting a Gaussian profile to each lesion image and averaging the standard deviation of this profile over the three lesions.

Setup	Lesion	Phase 2 CNR	Phase 3 CNR	Phase 2 average sigma (mm)	Phase 3 average sigma (mm)
Low-resolution detector	10% higher lesion density	2.4	1.7	3.3	3.5
	5% higher lesion density	1.4	0.8		
	5% lower lesion density	1.8	1.2		
Medium-resolution detector	10% higher lesion density	1.9	1.2	2.8	2.9
	5% higher lesion density	1.1	0.4		
	5% lower lesion density	1.4	0.9		
High-resolution detector	10% higher lesion density	1.1	0.7	2.5	2.7
	5% higher lesion density	0.4	0.3		
	5% lower lesion density	0.9	0.5		

TABLE V. Comparison between liver lesion locations in the gold standard and realistic registrations. The low-resolution detector setup has significantly higher registration error than the medium- and high-resolution setups. The medium- and high-resolution setups produce comparable-quality registrations. The registrations of the 5% higher density lesions have consistently higher error than those of the other two lesions. This may be caused by artifacts from the beam-hardening correction.

Setup	Phase 1/phase 2 (diagnostic/helical) registration: liver lesion center error (mm)	Phase 2/phase 3 (helical/axial) registration: liver lesion center error (mm)
Low-resolution detector	10% higher lesion density: 1.4 5% higher lesion density: 5.9 5% lower lesion density: 3.0	10% higher lesion density: 3.6 5% higher lesion density: 5.1 5% lower lesion density: 4.1
Medium-resolution detector	10% higher lesion density: 1.0 5% higher lesion density: 3.6 5% lower lesion density: 0.6	10% higher lesion density: 2.8 5% higher lesion density: 2.2 5% lower lesion density: 2.4
High-resolution detector	10% higher lesion density: 1.4 5% higher lesion density: 3.0 5% lower lesion density: 1.0	10% higher lesion density: 3.5 5% higher lesion density: 2.8 5% lower lesion density: 3.6

To examine the registration on a pointwise level, the registered locations of the centers of the three liver lesions in the realistic data were compared with the corresponding registered locations in the gold standard data. Table V shows the magnitude of the distance between these locations for each case. The phase 1 (diagnostic-quality)/phase 2 (helical) data show that the 10% denser and 5% less dense lesions were consistently registered more successfully than the 5% denser lesions. This may have been caused by the beam-hardening correction, which makes the liver tissue appear slightly too dense, an effect that was observed in all three phase 2 datasets. This decreased the relative contrast of the 5% denser lesion and thus decreased the likelihood that MIM would recognize the lesion as a unique feature. This result could possibly be improved by using a different type of beam-hardening correction.

In the phase 1/phase 2 registration, the registered 10% denser and 5% less dense lesion locations in all three realistic datasets were fairly close to the gold standard registered locations. Most notably, the registrations from the medium- and high-resolution detectors placed these lesions less than 1.5 mm away from their positions in the gold standard registration. This means that for this specific case, a radiotherapy treatment plan including a 1.5 mm margin of error around the lesions would successfully irradiate the entire lesion. However, a more rigorous quantification of random and systematic error is necessary to draw conclusions about the general case. The registrations from the medium-resolution detector dataset were slightly better than the registrations from the high-resolution detector dataset, which may have been caused by the reduced noise in the medium-resolution reconstruction relative to the high-resolution reconstruction.

The pointwise results of the phase 2 (helical)/phase 3 (axial) registration were uniformly worse than the results of the phase 1/phase 2 registration. The dataset from the medium-resolution detector performed the best, with a registered location error less than 3 mm for all three lesions. It is likely that in combination with the cone beam artifacts, the images from the low- and high-resolution detectors were too blurred and too noisy respectively to produce a good registration.

4. CONCLUSION

In summary, the data from the low-resolution detector nearly always produced registrations inferior to those of the medium- and high-resolution detectors, and thus, the low-resolution detector is not a good choice for a high-speed radiotherapy on-board imaging system. Overall, the medium- and high-resolution detectors produced images that could be registered with comparable success. Qualitatively, the deformation fields from the medium- and high-resolution detectors were of comparable similarity to the gold standard deformation field in both the phase 1 (diagnostic-quality)/phase 2 (helical) registration and the phase 2 (helical)/phase 3 (axial) registration. The pointwise distance between the medium-resolution detector's deformation field and that of the gold standard deformation field was larger than that of the high-resolution detector by almost every metric, but the differences in error were consistently less than 1 mm. In the point of interest error evaluation, the medium-resolution detector's deformation field outperformed the high-resolution detector's deformation field in almost every case, but again, the differences in lesion position error were consistently less than 1.5 mm. Given the comparable results of the medium- and high-resolution detectors, we believe that the medium-resolution detector provides a good balance between image quality and cost.

There is still work to be done in designing the on-board imaging system discussed in this study. First, it must be verified that the registration results presented here can be extended to real patient data. This could be confirmed by repeating the simulation procedure discussed in this study but substituting clinical CT reconstructions of a real patient for the numerical phantom. This would verify that textured surfaces such as real human organs can be registered accurately. The combination of fast, on-board CT imaging and extremely rapid radiation therapy may also permit use of contrast agents such as intravas-

cular iodine-based contrast, which may permit further reduction of dose while maintaining high-fidelity registration. The registration must also be examined in more detail in order to optimize the algorithm and develop a method to quantitatively evaluate individual registrations. Finally, the imaging hardware must be built and integrated with the radiation therapy hardware before the device can be tested and used in the clinic.

Once these steps are complete, the system will represent a significant step forward in optimizing speed, patient comfort, and accuracy in radiation therapy. Instead of being manipulated and restrained to match their position on the day of diagnostic imaging, patients can lie on the treatment table naturally and hold their breath for only a few seconds at a time while their treatment is adapted to their current position and delivered.

ACKNOWLEDGMENTS

a)Author to whom correspondence should be addressed. Electronic mail: mengwu@stanford.edu

[1]S. S. Korreman, "Motion in radiotherapy: Photon therapy," Phys. Med. Biol. **57**, R161–R191 (2012).

[2]S. A. Nehmeh and Y. E. Erdi, "Respiratory motion in positron emission tomography/computed tomography: A review," Semin. Nucl. Med. **38**, 167–176 (2008).

[3]C. Bert and M. Durante, "Motion in radiotherapy: Particle therapy," Phys. Med. Biol. **56**, R113–R144 (2011).

[4]E. Reitzel and C. Bert, "Respiratory motion management in particle therapy," Med. Phys. **37**(2), 449–460 (2010).

[5]P. J. Keall, G. S. Mageras, J. M. Balter, R. S. Emery, K. M. Forster, S. B. Jiang, J. M. Kapatoes, D. A. Low, M. J. Murphy, B. R. Murphy, C. R. Ramsey, M. B. Van Herk, S. S. Vedam, J. W. Wong, and E. Yorke, "The management of respiratory motion in radiation oncology report of AAPM Task Group 76," Med. Phys. **33**(10), 3874–3900 (2006).

[6]B. W. Loo, Jr., P. G. Maxim, and V. A. Dolgashev, "Pluridirectional very high electron energy radiation therapy systems and processes," U.S. patent 9018603 (28 April 2015).

[7]M. Bazalova-Carter, B. Qu, B. Palma, B. Hardemark, E. Hynning, C. Jensen, P. G. Maxim, and B. W. Loo, Jr., "Treatment planning for radiotherapy with very high-energy electron beams and comparison of VHEE and VMAT plans," Med. Phys. **42**(5), 2615–2625 (2015).

[8]M. Bazalova-Carter, M. Liu, B. Palma, M. Dunning, D. McCormick, E. Hemsing, J. Nelson, K. Jobe, E. Colby, A. C. Koong, S. Tantawi, V. Dolgashev, P. G. Maxim, and B. W. Loo, Jr., "Comparison of film measurements and Monte Carlo simulations of dose delivered with very high-energy electron beams in a polystyrene phantom," Med. Phys. **42**(4), 1606–1613 (2015).

[9]J. Zhu, "Feasibility of using cone-beam CT to verify and reposition the optically guided target localization of linear accelerator based stereotactic radiosurgery," Med. Phys. **38**(1), 390–396 (2011).

[10]U. V. Elstrom, L. P. Muren, J. B. B. Petersen, and C. Grau, "Evaluation of image quality for different kV cone-beam CT acquisition and reconstruction methods in the head and neck region," Acta Oncol. **50**, 908–917 (2011).

[11]S. Yoo and F. F. Yin, "Dosimetric feasibility of cone-beam CT-based treatment planning compared to CT-based treatment planning," Int. J. Radiat. Oncol., Biol., Phys. **66**(5), 1553–1561 (2006).

[12]G. X. Ding, D. M. Duggan, C. W. Coffey, M. Deeley, D. E. Hallahan, A. Cmelak, and A. Malcolm, "A study on adaptive IMRT treatment planning using kV cone-beam CT," Radiother. Oncol. **85**, 116–125 (2007).

[13]P. Alaei, "Review of the doses from cone beam CT and their inclusion in the treatment planning," AAMD 35th Annual Meeting, 2010.

[14]M. J. Murphy, Z. Wei, M. Fatyga, J. Williamson, M. Anscher, T. Wallace, and E. Weiss, "How does CT image noise affect 3D deformable image registration for image-guided radiotherapy planning?," Med. Phys. **35**(3), 1145–1153 (2008).

[15]J. Westberg, H. R. Jensen, A. Bertelsen, and C. Brink, "Reduction of cone-beam CT scan time without compromising the accuracy of the image registration in IGRT," Acta Oncol. **49**, 225–229 (2010).

[16]R. Boggula, F. Lorenz, Y. Abo-Madyan, F. Lohr, D. Wolff, J. Boda-Heggemann, J. Hesser, F. Wenz, and H. Wertz, "A new strategy for online adaptive prostate radiotherapy based on cone-beam CT," Z. Med. Phys. **19**, 264–276 (2009).

[17]D. Paquin, D. Levy, and L. Xing, "Multiscale registration of planning CT and daily cone beam CT images for adaptive radiation therapy," Med. Phys. **36**(1), 4–11 (2009).

[18]M. Thor, J. B. B. Petersen, L. Bentzen, M. Hoyer, and L. P. Muren, "Deformable image registration for contour propagation from CT to cone-beam CT scans in radiotherapy of prostate cancer," Acta Oncol. **50**, 918–925 (2011).

[19]M. Zarepisheh, T. Long, N. Li, Z. Tian, H. E. Romeijn, X. Jia, and S. B. Jiang, "A DVH-guided IMRT optimization algorithm for automatic treatment planning and adaptive radiotherapy replanning," Med. Phys. **41**(6), 061711 (14pp.) (2014).

[20]U. V. Elstrom, B. A. Wysocka, L. P. Muren, J. B. B. Petersen, and C. Grau, "Daily kV cone-beam CT and deformable image registration as a method for studying dosimetric consequences of anatomic changes in adaptive IMRT of head and neck cancer," Acta Oncol. **49**, 1101–1108 (2010).

[21]P. Alaei, G. Ding, and H. Guan, "Inclusion of the dose from kilovoltage cone beam CT in the radiation therapy treatment plans," Med. Phys. **37**(1), 244–248 (2010).

[22]W. P. Segars, G. Sturgeon, S. Mendonca, J. Grimes, and B. M. W. Tsui, "4D XCAT phantom for multimodality imaging research," Med. Phys. **37**(9), 4902–4915 (2010).

[23]Y. Long, J. A. Fessler, and J. M. Balter, "3D forward and back-projection for x-ray CT using separable footprints," IEEE Trans. Med. Imaging **29**(11), 1839–1850 (2010).

[24]M. Gies, W. A. Kalender, H. Wolf, C. Suess, and M. T. Madsen, "Dose reduction in CT by anatomically adapted tube current modulation. I. Simulation studies," Med. Phys. **26**(11), 2235–2247 (1999).

[25]A. Badal and A. Badano, "Fast and accurate estimation of organ doses in medical imaging using a GPU-accelerated Monte Carlo simulation code," Med. Phys. **38**(6), 3411 (2011).

[26]J. H. Siewerdsen, A. M. Waese, D. J. Moseley, S. Richard, and D. A. Jaffray, "Spektr: A computational tool for x-ray spectral analysis and imaging system optimization," Med. Phys. **31**(11), 3057–3067 (2004).

[27]B. Meng, H. Lee, L. Xing, and B. P. Fahimian, "Single-scan patient-specific scatter correction in computed tomography using peripheral detection of scatter and compressed sensing scatter retrieval," Med. Phys. **40**(1), 011907 (12pp.) (2013).

[28]L. Feldkamp, L. Davis, and J. Kress, "Practical cone-beam algorithm," J. Opt. Soc. Am. A **1**(6), 612–619 (1984).

[29]H. Kudo, T. Rodet, F. Noo, and M. Defrise, "Exact and approximate algorithms for helical cone-beam CT," Phys. Med. Biol. **49**(13), 2913–2931 (2004).

[30]X. Tang, J. Hsieh, R. A. Nilsen, S. Dutta, D. Samsonov, and A. Hagiwara, "A three-dimensional-weighted cone beam filtered backprojection (CB-FBP) algorithm for image reconstruction in volumetric CT-helical scanning," Phys. Med. Biol. **51**(4), 855–874 (2006).

[31]J. Hsieh, E. Chao, J. Thibault, B. Grekowicz, A. Horst, S. McOlash, and T. J. Myers, "A novel reconstruction algorithm to extend the CT scan field-of-view," Med. Phys. **31**(9), 2385–2391 (2004).

[32]S. S. Hsieh, G. Cao, B. E. Nett, and N. J. Pelc, "Truncation artifact correction by support recovery," Proc. SPIE **8668**, 86683N-1–86683N-6 (2013).

[33]A. Sotiras, C. Davatzikos, and N. Paragios, "Deformable medical image registration: A survey," IEEE Trans. Med. Imaging **32**(7), 1153–1190 (2013).

[34]A. Neff, personal communication (2014).